

First Reliability Test of a Surface Micromachined Microengine Using SHiMMeR

Danelle M. Tanner, Norman F. Smith, Duane J. Bowman,
William P. Eaton, and Ken A. Peterson

Sandia National Laboratories, P. O. Box 5800, MS 1081, Albuquerque, NM 87185-1081

ABSTRACT

The first-ever reliability stress test on surface micromachined microengines¹ developed at Sandia National Laboratories (SNL) has been completed. We stressed 41 microengines at 36,000 RPM and inspected the functionality at 60 RPM. We have observed an infant mortality region, a region of low failure rate (useful life), and no signs of wearout in the data. The reliability data are presented and interpreted using standard reliability methods. Failure analysis results on the stressed microengines are presented. In our effort to study the reliability of MEMS, we need to observe the failures of large numbers of parts to determine the failure modes. To facilitate testing of large numbers of micromachines, we designed and built an automated system that has the capability to simultaneously test 256 packaged micromachines. The Sandia High Volume Measurement of Micromachine Reliability (SHiMMeR) system has computer controlled positioning and the capability to inspect moving parts. The development of this parallel testing system is discussed in detail.

Keywords: micro-mechanical component reliability, micromachine reliability, failure in micromachines, MEMS reliability

1. INTRODUCTION

As MicroElectricalMechanical Systems (MEMS) become deployed in more commercial applications, understanding the reliability issues will be paramount for success. Complicating MEMS reliability is the fact that reliability issues and the associated failure modes of MEMS are not well characterized. Furthermore, reliability issues may be very sensitive to the type of component and the fabrication technology, so that different mechanisms must be identified for sensors and actuators or among surface micromachined, bulk micromachined, and high aspect-ratio micromachined (HARM) parts. While there is a lack of knowledge base for reliability of MEMS, there is some guidance in the literature. There has been some work reported on the reliability testing of sensors^{2,3,4} and specifically those that are exposed to harsh environments.⁵ Additionally, a study of the reliability of cantilever beams has also been reported.⁶ There

has also been a report of reliability for actuators based upon crack propagation in polysilicon.⁷

In any reliability study, the application of the product determines the types of testing that should be done. For example, different environmental tests are required for an automotive product than a product with a space application.⁸ In this paper, we examine the reliability of an actuator, the SNL microengine (described in detail in section 3). Our approach is to test a statistically significant number of parts to failure in order to identify dominant failure mechanisms. Our overall goal is to determine acceleration factors for these failure mechanisms (e.g. temperature, humidity, etc.) to formulate a reliability model which will predict nominal part lifetimes based on accelerated testing data. The work described in this paper was the development of the infrastructure needed to begin our reliability studies.

2. SHiMMeR DESIGN

2.1 Optical System

The Sandia High Volume Measurement of Micromachine Reliability (SHiMMeR) system was designed and built to provide electrical drive signals to large numbers of packaged microactuators and to optically inspect them for functionality. SHiMMeR is subdivided into the electrical subsystem, which provides optimized electrical signals to the packaged parts and the optical subsystem, in which a microscope and camera are stepped from part to part to inspect functionality. The optical system for SHiMMeR consists of three major components, an X-Y gantry table, a video microscope and automatic data recording/assembly (Figure 1). The X-Y gantry table used to build the SHiMMeR system is a Techno Isel Gantry System III table with a travel of 500 x 540 mm, a table size of 850 x 750 mm, and a 200mm clearance under the Z axis. This table has a repeatability of 10 μ m and can support a payload of 22.7kg on the Y axis. The axes are driven by Parker Compumotor Indexers that provide a resolution of 1.25 μ m, when used with the standard 5mm pitch ball screw on the table. The overall accuracy of the table is ± 0.1 mm over 300 mm. A high accuracy table was not required for this application because the MEMS device has considerable variation when it is mounted inside

its package and where it is placed in the test fixture. These variations prevent exact determination of where the part is located within the travel of the gantry table, thus negating the requirement for accurate linear distance moves. Currently the operator of the SHiMMeR system is required to manually teach the system the location of each MEMS device being characterized.

The video microscope used in SHiMMeR is a 9x A-Zoom microscope from Ready Products Corporation. This microscope has many features that made it a very useful in our system. It uses a single lens for its entire magnification range. In our configuration, with a 20x long working distance objective, the magnification is continuously variable from 250x to 1800x with a field of view ranging from 1.1 mm to 150 μm on a 13 inch monitor. This allows the SHiMMeR system to look at a wide variety of MEMS devices without the operator having to change primary objectives, thus eliminating the possibility that a turret full of lenses would collide with other parts of the system. The microscope is equipped with motorized focus controls and illumination is provided through a 150W fiber optic light source. All aspects of the microscope can be controlled from a personal computer via an RS-232 port. A high resolution black and white CCD camera is used for acquisition of the image.

The automatic data recording subsystem consists (see Figure 2) of a pair of video cassette recorders (VCR) and a character generator. All components of this sub-system are controlled via RS-232 communications. Device operation is recorded during the manual inspection portion of the stress. This data is recorded continuously for all devices under test to one of the VCR's. After completion of the experiment, the raw recorded data is processed into a format suitable for self-documentation of the test. This post-experiment processing consists of dubbing the continuously recorded tapes into a continuous tape segment of each device being tested, with text overlays describing what the test operator observed during testing.

2.2 Stimulus System

The stimulus or stressing system is made up of several components: waveform synthesis, waveform amplification, waveform distribution, and MEMS device fixtures. Waveforms for driving the MEMS devices are created using four 20 MHz arbitrary waveform generators from Pragmatic Instruments. All four channels are phase-locked together and use a common clock. Custom waveforms are downloaded via IEEE-488.2 bus to the waveform generators. These waveform generators allow multiple waveforms to be sequenced together to generate acceleration and decelera-

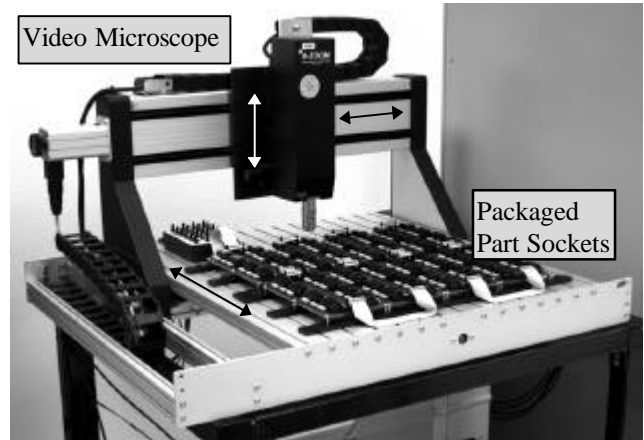


Figure 1. The X-Y gantry table showing the socket arrangement and video microscope. The arrows indicate possible motion direction.

tion profiles required for high speed operation of the SNL microengines⁹.

The maximum output voltage from the waveform generators is limited to $\pm 10\text{V}$. Since this voltage is insufficient to actuate the electrostatic comb drives of the SNL microengine, the output waveforms must be amplified to a voltage sufficient to drive the device. Amplification is achieved with a custom 4-channel amplifier designed and built at SNL. The amplifier provides up to a 200V drive signal for the electrostatic combs and has a bandwidth sufficient to drive the microengines up to 600,000 rpm. The current speed record for the microengine devices discussed in this paper is 309,000 rpm.¹⁰

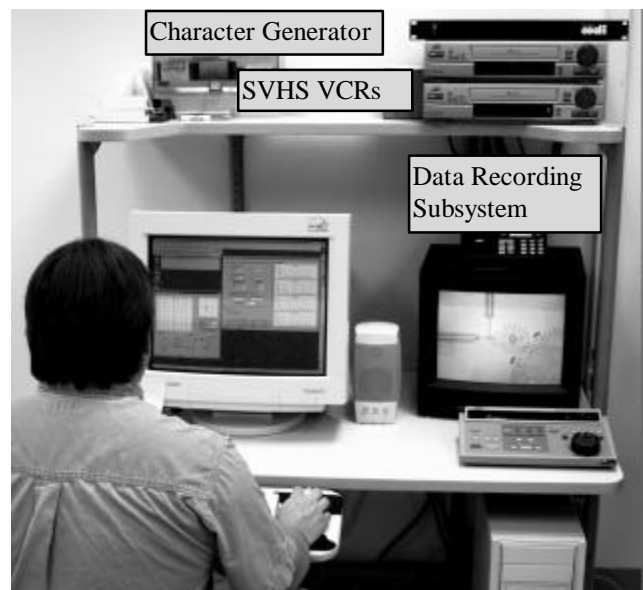


Figure 2. Software control and data recording subsystem of the SHiMMeR system. The operator is author Norman Smith.

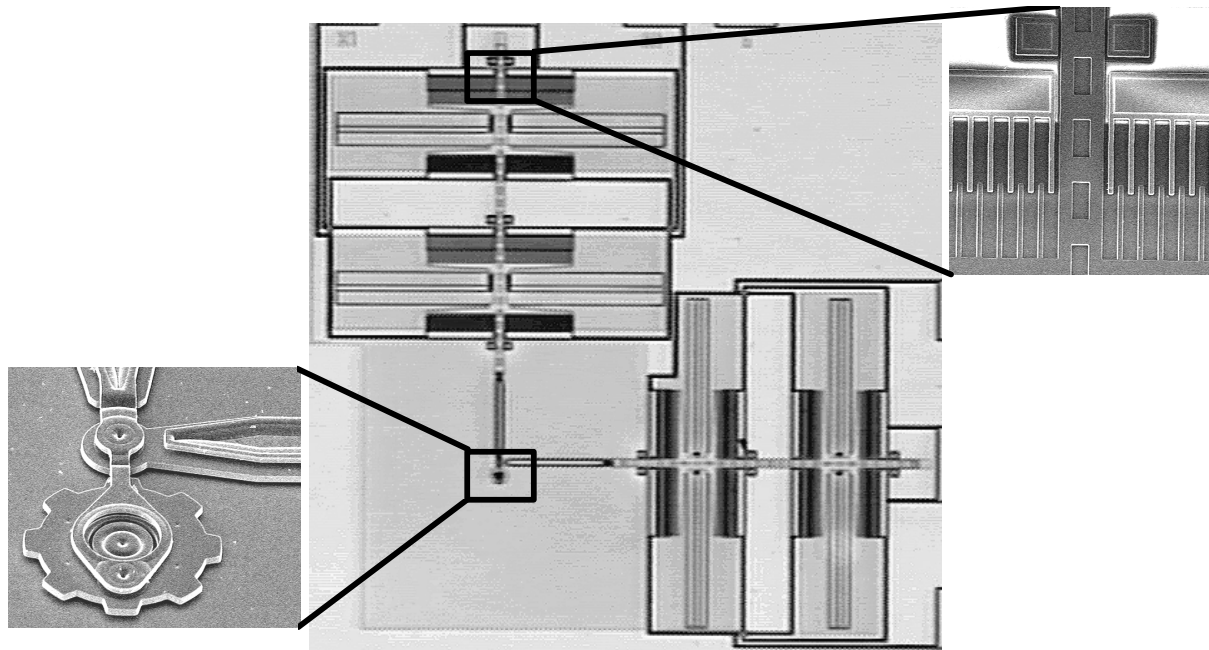


Figure 3. The microengine with expanded views of the comb drive (top right) and the rotating gear (bottom left) shown in what we define as the 6 o'clock position..

The device fixture consists of modular printed circuit boards with 8 24-pin DIP sockets. All sockets on the board are wired in parallel with each pin isolated from the parallel bus via 1 M Ω resistors. This provides the needed isolation from one device short circuiting and causing the remaining devices to stop functioning due to missing drive signals. The test bed consists of a 4 x 2 array of these printed circuit boards (see Figure 1). This arrangement of multiple small printed circuit boards, rather than one large board provides great flexibility in the arrangement, device wiring, and signal optimization of MEMS devices under test.

Waveform distribution is controlled through a manual switch matrix. The current matrix is arranged in a 6 x 24 arrangement. The arrangement accommodates the four drive signals required for the SNL microengine, a ground line, and a line that disconnects the socket pin from any signal.

2.3 Software

The software developed to run the SHiMMeR system was written at SNL using Visual Basic. This software allows the operator to optimize and vary all engine drive signal parameters. The drive signals were viewed on the monitor, before application to the devices under test. Any test fixture arrangement that can be made to fit within the travel of the X-Y gantry table as well as any layout of the MEMS device can be accommodated through simple description files created by the software. The operator test screen allows stress and duration parameters to be defined and varied throughout the test. A running commentary can be kept on each device under test until it fails, at which time the software will skip the observation portion of the test unless set up to

do otherwise. Device failures are currently broken down into three major categories where each category can have one level of sub-categories. The operator can use the predefined sub-categories or add additional ones as the test progresses. A color coded map of the test bed shows the operator the current status of each package under test as well as the status of each device in each package.

3. EXPERIMENT

The structure tested was the SNL microengine which consists of orthogonal linear comb drive actuators mechanically connected to a rotating gear as seen in Figure 3. These microengines are a useful test vehicle to identify failure modes and methods since they possess the rotational/sliding friction components found in many devices. Based on previous work⁹, quantifying the process of degradation by observing the changes in behavior of the microengine to failure should yield significant results.

In our experiment to study a statistically significant number of microengines, 52 packages with glass observation covers were mounted in the device fixture boards of the X-Y gantry table. The unsealed covers prevented particle contamination, however the microengines were exposed to the ambient environments of temperature and humidity of the laboratory.

There were four microengines, representing different pin joint or flex joint combinations, on each die attached in each package. In our initial scan to check functionality, we identified 41 working engines to perform the stress test.

The stress test involves a repeated process of stressing the engines at 36,000 RPM for a defined number of revolutions and then observing functionality at 60 RPM. The stress speed of 36,000 RPM was chosen to be below the resonance of the comb drives. In the transition from one speed to the other, we decelerated in one revolution, momentarily stopped the gear (for roughly one second) and then accelerated, again in one revolution, to the other speed. We made the assumption that the stress during the observation period was negligible.

Our criteria for a failed part was the inability to complete a revolution (cycle). During the observation period, we made a decision about the functionality of the engine, flagged the failed engine or commented on the motion of a functioning engine, and recorded the motion of the microengine on video for post test analysis.

At the beginning of the test we stressed for a short duration expecting the weaker parts to fail quickly. As the test progressed, the duration of the stress was increased. The entire test lasted for 28 days with a total of 32 separate stress periods.

The progression to failure was similar in most of the micro-engines that we observed. The gear went from rotating smoothly to momentarily sticking but completing a revolution. This erratic behavior then led to either the gear oscillating, typically between the 7 o'clock and 11 o'clock positions, or freezing in one position.

4. RESULTS AND DISCUSSION

4.1 Data Analysis

The long term reliability test resulted in a total of 1.1 billion "stress" cycles (revolutions) on the longest running engines. Because the parts were observed at fixed inspection times, common to all the parts, the results fall in the category of reliability data called "interval" data. This is also commonly known as "grouped" or "inspection" data. Useful methods for analyzing this type of data are documented in Nelson^{11,12} and Peck.¹³

Of the 41 working engines that started the test, 36 eventually failed. They exhibited a decreasing failure rate, with no sign of wearout evident in the data. Figure 4 shows two separate views of the same estimated hazard rate (i.e. instantaneous failure rate) data from this test. The units on the vertical axis are failures expressed in parts per million (ppm) cycles, i.e. the estimated number of failures that would be expected in one million total device-cycles. This data is "smoothed" by averaging any failures over the stress interval since the last observed failure, providing a conceptual plot of the decreasing failure rate typically associated

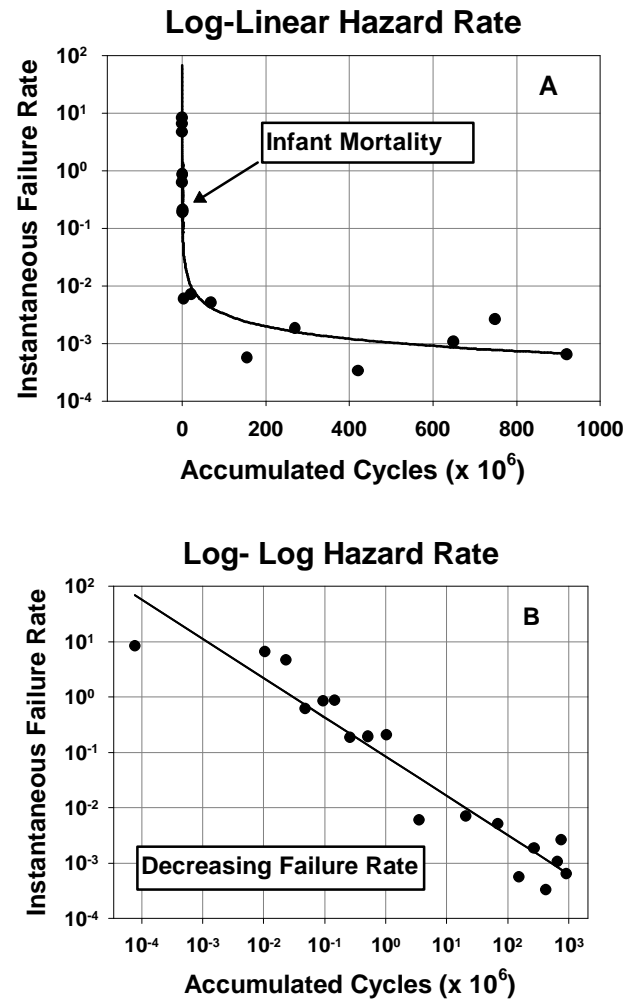


Figure 4. The instantaneous failure rate was plotted on different scales. The top curve (A) shows the early failure infant mortality region. The bottom curve (B) shows a more detailed representation of the decreasing failure rate throughout the life test.

with the first part of the familiar "bathtub" curve. The "accumulated cycles" axis represents the geometric mid-points in the stress intervals, which is a somewhat arbitrary choice of where to assign the failure times, but consistent with the observed dependency of failure rate on logarithmic time. Figure 4A uses a linear "accumulated cycles" scale to illustrate a generally decreasing failure rate up to about 1 billion cycles; Figure 4B uses a log-log scale to show the decreasing tendency in failure rate throughout the life test.

The fact that a straight line could be reasonably fit through the data on the log-log plot of Figure 4B indicates that an inverse power-law can describe the hazard rate, and in fact the Weibull distribution for decreasing failure rates has a hazard rate function of that form. This curve is primarily

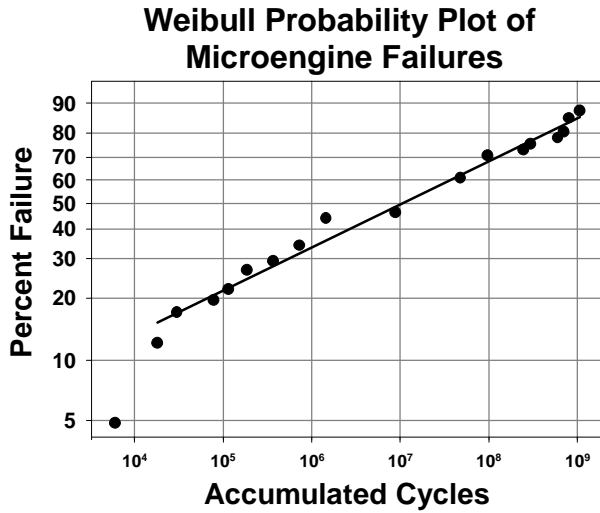


Figure 5. Microengine failure data fit to a Weibull distribution.

meant to be illustrative of a generally decreasing failure rate, and is not a robust curve from which to derive a distribution model. Figures 5 & 6 show attempts to fit the data to classical distribution models.

4.1.1 Weibull Distribution

Figure 5 depicts the fit of our microengine failure data to the Weibull distribution model. The resulting straight line fit indicates that the Weibull distribution is a reasonable model for cycles-to-failure of these devices. The Weibull fit results in an estimate for the "characteristic life" of $\alpha = 66$ million cycles (the characteristic life is defined as the point in time when $(1-e^{-1})$ 100% = 63.2% of the parts are expected to fail), and an estimate for the shape parameter of $\beta = 0.22$. The shape parameter is essentially a measure of dispersion, and lower values correspond to greater spread in logarithmic lifetime. Typical values of β for production-ready electronic and mechanical products fall in the range of 0.5 to 5. The considerably wide dispersion in lifetimes for the microengines is to be expected because there is still considerable process learning to occur in this infant technology.

One very useful aspect of the Weibull distribution is that values of the shape parameter below $\beta = 1$ correspond to a consistently decreasing failure rate; if the failure rate were to transition to a constant or increasing failure rate, a bimodal distribution would then be observed in the distribution fit, with the additional modes showing $\beta \geq 1$, i.e. a different slope. Hence, the Weibull fit confirms that the failure rate is decreasing throughout this life test, and is consistent with the inverse power law form of the hazard rate estimates in Figures 4.

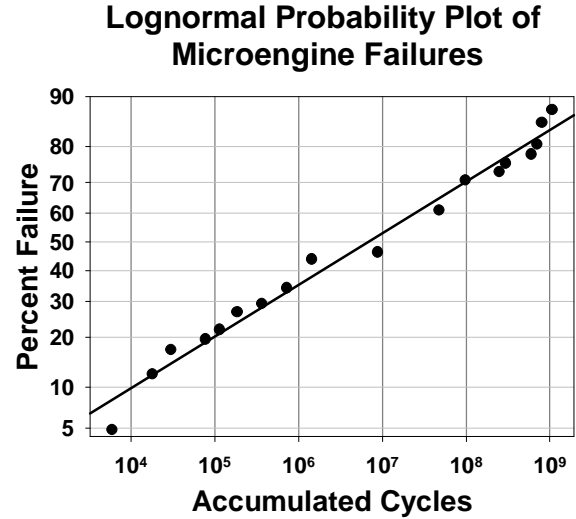


Figure 6. Microengine failure data fit to a lognormal distribution.

4.1.2 Lognormal Distribution

Figure 6 depicts the fit of our microengine failure data to the lognormal distribution model. The resulting straight line fit indicates that the lognormal distribution is also a reasonable model. The lognormal fit results in an estimate of a median lifetime of $t_{50\%} = 7,800,000$ cycles, which means that 50% of the parts would be expected to fail by 7,800,000 cycles. The estimate for the lognormal shape parameter is $\sigma = 5.2$. In this case, the relatively high value of the lognormal standard deviation again indicates a large spread in the log lifetimes. Typical semiconductor products show lognormal standard deviations in the range of 0.1 to 1.0.

In the case of the lognormal distribution fit it is not simple to determine if the failure rate is decreasing, constant or increasing, since the lognormal distribution can manifest all of these in a single unimodal case. By physical argument, it is reasonable to expect that a transition from infant mortality (decreasing failure rate) to wearout (increasing failure rate) would be due to a change in physical failure mechanism and bimodality would be observed in the distribution fit. Still, increasing and decreasing failure rates cannot be easily discriminated on a lognormal probability plot.

4.1.3 Discussion of the Results

Across the range of failure probability estimates generated from this data, the two distributions turn out to be almost indistinguishable, i.e. the Weibull and lognormal distributions both fit the observed data equally well. In fact, visual comparisons of the probability density function, cumulative distribution functions and failure rate plots of the lognormal distribution (in the high σ case) and the Weibull distribu-

tion (in the low β case) show that they can have very similar shapes.¹³ So, with consistent characteristic lifetimes (as is necessarily the case here, since we are using the same data) and the respective shape parameters that were derived from the lognormal and Weibull distribution fits, the two distributions are evidently nearly indistinguishable across the observed range of failure data.

The fact that the failure rate is consistently decreasing indicates that the parts contain defects that result in the observed failures. This "weeding out" process is typically called infant mortality and necessarily results in a decreasing failure rate because each loss of a defective part renders the remaining sample more defect-free. The typical failure modes of the microengines appears to be a stiction event of the spinning gear, resulting in a stuck or oscillating gear. Efforts to understand the failure mode will be discussed in the failure analysis section. At this point it is not clear what is causing the gear to stop spinning; however, subject to the caveat explained in the next section, it appears that the stiction event is brought on by pre-existing defectivity in the microengines. If the stiction were due to accumulation of wear caused by excessive rubbing, in the absence of major defectivity, the failure rate would necessarily increase as the parts accumulate stress.

Another implication of the observed decreasing failure rate is that effective burn-in schedules can be devised, once the manufacturing process is sufficiently under control that stationary statistics can be applied. The goal would then be to weed out enough defective parts that the failure rate of the remaining parts is acceptably low, usually expressed as a FIT (failures-in-time) or ppm (parts per million) requirement. Such a burn-in schedule would have to be periodically supplemented by long-term life tests to ensure that wearout (increasing failure rates) never starts occurring unacceptably soon, impinging on the required lifetime of the parts.

There is one potentially important caveat to the conclusions stated, and that lies in the method in which the data was obtained. As explained previously, the parts were stressed at high speed (36000 rpm), and then slowed down to a slow speed (60 rpm) to observe their operation. In fact, due to the nature of the experimental apparatus, the engines were actually decelerated to a stop for one second during any transition in speed. The analysis presented in this paper assumes that degradation accumulated during the high speed "stress" intervals, and was negligible during the slow speed inspection intervals, the very brief pauses, and the deceleration and acceleration periods. (This is analogous to the concerns raised commonly in product life tests when parts that are stressed at high temperature are brought down

to room temperature for inspection, resulting in undesired thermal cycling.) An attempt to analyze the failure data as a function of these deceleration, stop, slow speed, stop, acceleration cycles was inconclusive, but showed a generally constant failure rate.

A constant failure rate is indicative of a failure mechanism that has no "memory", i.e. it is due to random external events and is not heavily influenced by defectivity or wear. For example, the chance encounter of obstructing contaminant particles with sliding surfaces could result in a constant failure rate, if the likelihood of such encounters were nearly equal for all microengines. Hence, there remains the possibility that the decreasing failure rate reported here is an artifact of the approximately logarithmic "stress" intervals that were chosen for the test. Alternatively, the data reported here may represent a composite degradation due to two or more of these possible causes. Therefore, we plan to do a follow-up experiment which will be designed to separate out any and all effects due to these various speed conditions.

4.2 Failure Analysis

Failure analysis is an ongoing activity on these samples, but some preliminary results are included here. Tools and techniques employed in prior work¹⁴ include optical microscopy, focused ion beam (FIB) cross-sectioning, FIB excising of discrete elements, FIB imaging, laser cutting of discrete elements, scanning electron microscopy (SEM) with passive and active voltage contrast, atomic force microscopy, analysis of visible and infrared light emission, and acoustic microscopy. The analysis of MEMS is expected to drive novel implementations of these techniques and the development of new techniques.

Failure Analysis (FA) activities have consisted of examination of several failures from the first lifetime test. A significant complication in the failure analysis has been the inability to duplicate failures. The engines were operated for the purpose of FA by four half sine waves applied to the four drive terminals in 90° phase steps. After the failed microengines were delivered to FA, the behavior of many microengines had changed. As might be expected, several engines which were operating at the end of the test had ceased operating. More surprisingly, several engines which had failed by the end of the test, or which didn't perform well enough for inclusion in the test, demonstrated an improved operating condition. The only engines which were consistent were a subset of those which appeared to be stuck at some location on the microengine structure. "Stuck" as it is used here means surfaces adhering to each other (i.e., as opposed to failing to complete a revolution). Usually this is a permanent condition, however two types of exception

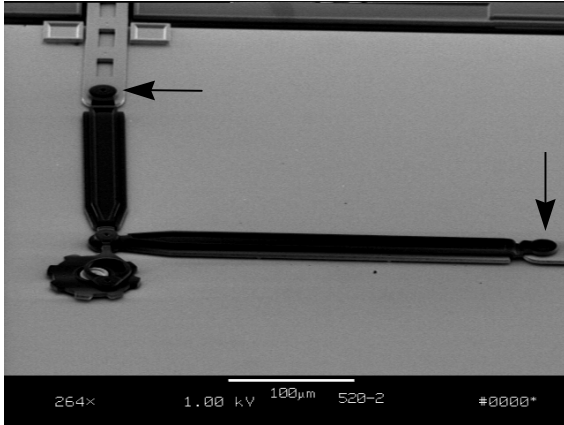


Figure 7. Passive voltage contrast image of pin joint micromachine showing charging of links, gear with respect to sample. Arrows show change of potential due to pin joints.

were observed. One may have been a failure mechanism wherein a gear stuck momentarily at some point in its rotation, and then freed itself due to a combination of increased force or mixed motion between rocking and rotation. A second is the reversible cyclic contact between opposing combs. Permanent lateral sticking of a single comb finger coincided with stopping the operation of two microengines during FA troubleshooting.

Two scanning electron microscopy (SEM) techniques, new in the application to MEMS, have been utilized to study the microengines. The first was passive voltage contrast (VC), where no external voltage was applied to the packaged part and all the pins were grounded. Contrast arose from the fact that electrically isolated elements attained a different potential, due to charge injection from the electron beam, than did grounded elements. The secondary electron yield, which was used to construct the image, depended on this potential. Figure 7 shows such an image at 1keV accelerating potential, where the isolated two link arms and gear charged to a positive potential with respect to the rest of the sample, resulting in a dark appearance of those elements. The shuttles were grounded through their springs, and the hub was grounded through its attachment to the substrate. The links and gear were only grounded if the physical contact at pin joints resulted in electrical contact, which was not occurring in this case. On the contrary, Figure 8 shows that the electrical connection provided by the flexible links

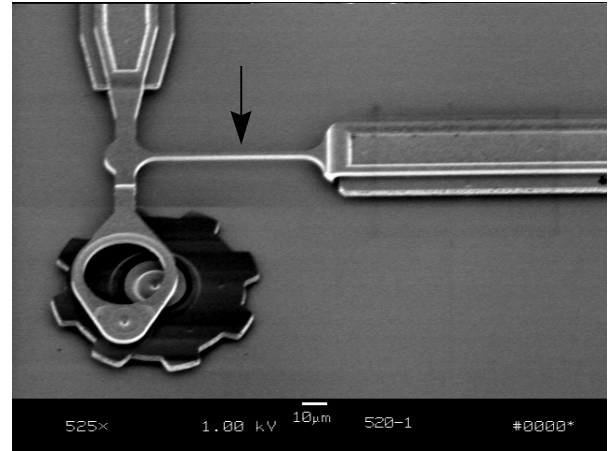


Figure 8. Passive voltage contrast of flexible link micromachine showing charging of gear with respect to links and the rest of the sample. Arrow shows flexible link.

drains charge from the link arms, but that the gear still charged positively, as it was not directly coupled to either the link arms or the hub.

Passive VC imaging also identified one comb drive and associated interconnect line which have charged to a positive potential with respect to the opposing comb drive and the rest of the sample, even though all the package pins were grounded. Figure 9 shows a darker appearance on the Y comb on the left, compared to the comb on the right, which is attached to the shuttle. Tracing this line in the SEM, the effect seemed to be due to the resistance of the line, as it gradually equilibrated toward the wirebonded pad. Figure 10 shows a crossover of lines feeding opposing combs, where the passive voltage contrast effect was still visible.

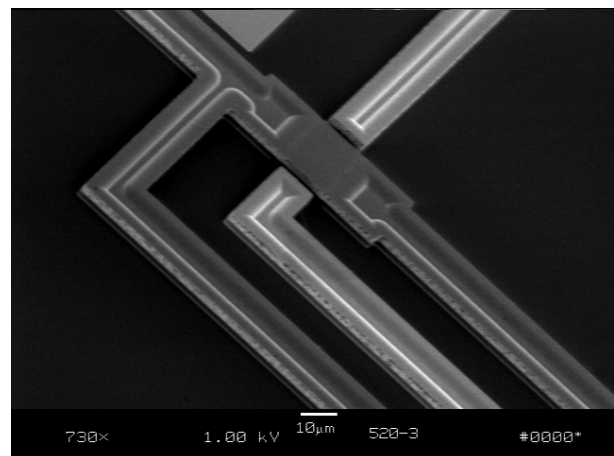


Figure 10. Voltage contrast at a crossover, showing charging of an interconnect line (all pins grounded).

The second new technique employed, was active voltage contrast, wherein external voltages were applied to micro-engine elements as they were examined in the SEM. The charging behavior of the electrically isolated elements of the operating microengines were observed with this technique. One gear which was electrically floating at rest changed as it was run counter-clockwise. It charged during the portion of its rotation from the 12:00 position to the 6:00 position, and then discharged and recharged during the portion from the 6:00 position to the 12:00 position. While the electron beam seemed to interfere significantly with a few microengines, as found in previous work, certain engines were successfully run for several hours in the SEM with no attempt to limit electron beam illumination to any portion of the microengine.

Voltage contrast has also been observed on static and operating microengines in the positive ion beam used in the FIB. More importantly, it has been demonstrated in the FIB that it is possible to electrostatically clamp a gear at high beam current, presumably when the positively charged gear is attracted to the grounded substrate. Charge neutralization (via an electron flood gun) has been used to mitigate the positive charging from the ion beam. Microengines have been observed to operate smoothly using charge neutralization, then fail to rotate when the neutralization is suspended. This is a reversible phenomenon.

Several microengines revealed elements which appeared to be stuck to the substrate at a single point. A confocal image of one such device was generated on a scanning optical microscope (SOM) and is shown in Figure 11. The Y link has a pin at one end which is accepted by a hole in the tip of the comb drive shuttle (point A). At the other end of the Y link is a hole which accepts a pin from the X link (point B). On this device, only the pin end of the Y link appeared to be stuck (point A). The comb drive shuttles were free and were reciprocating within the fabrication tolerance at respective pins. The pin in the gear was free and the gear was free on the hub. The end of the stuck link nearest the gear (point B) was free, which permitted the Y link to bend as the X link reciprocated. The height profile in Figure 11, however, showed the "stuck" end to be higher above the substrate than the free end. The link was examined in the scanning electron microscope with the result that no slope was resolved which supports a conclusion of sticking to the substrate at point A. This sample is a candidate for a focused ion beam (FIB) cross section in ongoing FA to examine the surfaces in question.

A confocal image of another defect is shown in Figure 12. This single comb drive finger in contact with the substrate coincided with a change in behavior from intermittent rotation to rocking back and forth. A scanning electron micro-

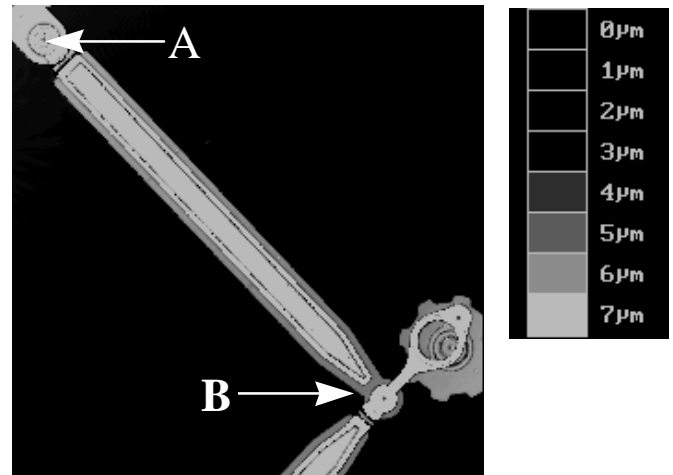


Figure 11. Confocal image of Y link which appears to be stuck at point A.

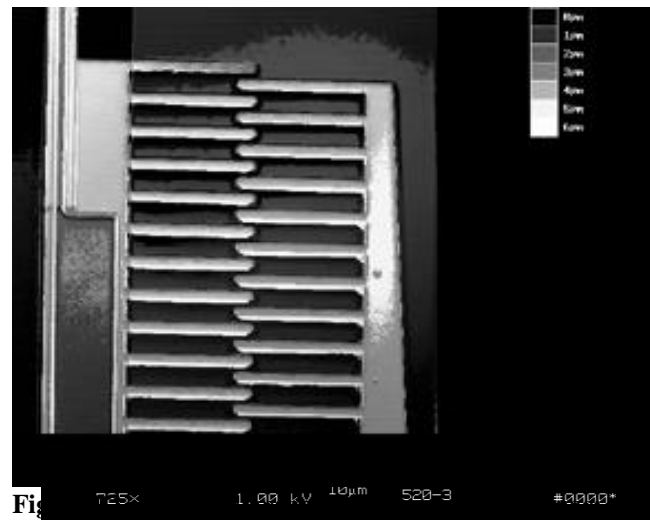


Figure 9. Voltage contrast showing charging of the comb on the left.

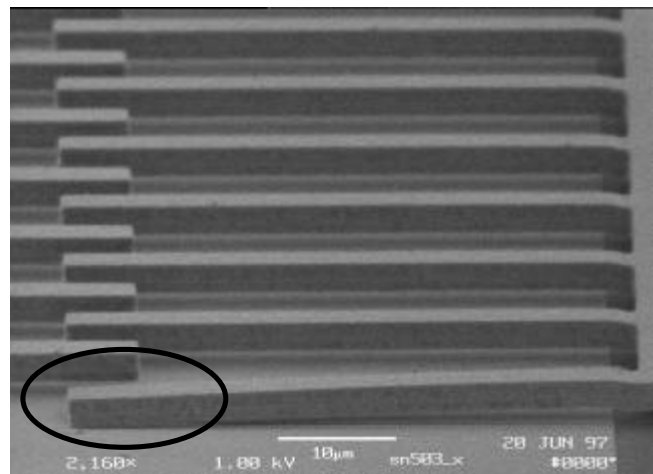


Figure 13. Stuck finger on comb drive.

scope image of the stuck finger is shown in Figure 13. This defect was associated with a $9K\Omega$ short between the comb and ground. The finger has been lifted by directing a cutting laser pulse, and the short is still present indicating presence of another defect.

Theories regarding stiction of micromachined surfaces due to charging effects and moisture are common in the literature. While operation in the SEM eliminates the possibility for the continued introduction of moisture, the injection of charge from the beam is an intrusive way to study charge effects. Future analysis will use a scanning probe microscope, which is ideal to non-intrusively study surface potential, and hence, charge effects of microengines, both at rest and in operation. An understanding of differences in surface potential may provide important clues to localizing anomalies in engine performance and help to identify root causes of engine failure. Microelectronic FA techniques are expected to improve the understanding of failure mechanisms for microengines.

5. CONCLUSIONS

We have demonstrated that our technique in using a high volume parallel testing system, SHiMMeR, yielded a successful long-term reliability lifetime test of the SNL microengine.

The microengine failure data showed no evidence of wearout in the distributions but there was a significant infant mortality region. The fact that both Weibull and lognormal distributions can be fit with a straight line indicates a unimodal failure distribution. This implies that there may have been only one dominant failure mode. This failure mode could have been large enough to overshadow any wearout.

This significant result of no wearout could indicate that microengines do not wear like macro devices. However, it could also mean that we just have not stressed the parts long enough since the record for revolutions of a SNL microengine is 3.2 billion.¹⁰

Several FA techniques developed for microelectronics have proven useful in the analysis of MEMS. The prevailing mode of failure was the gear sticking either to the substrate or to the hub. This was determined due to the presence of motion in the comb drives, but no translation of that motion to the gear. Voltage contrast in the SEM and in the FIB has been used to identify charging on the gears and links of stationary and operating engines. This charging may be related to the erratic behavior in the rotation of the microengine as observed in the FIB.

Future work on the SHiMMeR system includes the addition of an automated image analysis to lessen the burden on the test operator to determine failure criteria and to gather performance degradation data while the device is at its operational speed. Other possible additions to the system include a humidity controlled environment for the devices and an increased waveform generation capacity to allow the system to stress devices with variations in their drive signals simultaneously instead of sequentially.

ACKNOWLEDGMENTS

The authors thank Sam Miller and Bill Miller for their support in this study. We also thank the personnel of the Microelectronics development Laboratory at SNL for fabricating, releasing, and packaging the devices used in the test.

This work was supported by the United States Department of Energy under Contract DE-AC04-94AL85000. Sandia is a multiprogram laboratory operated by Sandia Corporation, a Lockheed Martin Company, for the United States Department of Energy.

REFERENCES

- ¹E. J. Garcia and J. J. Sniegowski, "Surface micromachined microengine", *Sensors and Actuators A*, **Vol. 48**, pp. 203-214 1995.
- ²T. Sasayama, S. Suzuki, S. Tsuchitani, A. Koide, M. Suzuki, T. Makazawa, and N. Ichikawa, "Highly Reliable Silicon Micromachined Physical Sensors in Mass Production", *Sensors and Actuators A*, **Vol. 54**, pp. 714-717, 1996.
- ³S. Bart, J. Chang, T. Core, L. Foster, A. Olney, S. Sherman, W. Tsarg, "Design Rules for a Reliable Surface Micromachined IC Sensor", *1995 IEEE International Reliability Physics Proceedings, IRPS 95*, pp. 311-317 (1995).
- ⁴S. Cunningham, "Reliability and Quality Assurance of MEMS Technology", *Micromachining Workshop III, Abstracts*, (Sept. 1996).
- ⁵T. Maudie, "Testing Requirements and Reliability Issues Encountered with Micromachined Structures", *Proceedings Of 2nd International Conference on Microstructures and Microfabricated Systems*, **95-27**, pp. 223-230, 1995.
- ⁶A. Rawicz, M. Parameswaran and J. M. Chen "Reliability and Yield in Fabrication of Microcantilever Structures using Bulk Silicon Micromachining", *Microelectronics Reliability*, **Vol. 36, No. 10**, pp. 1369-1374, 1996.
- ⁷S.B. Brown "Materials Reliability in MEMS Devices", *Technical Digest, 1997 International Conference of Solid-State Sensors and Actuators, Transducers '97*, pp. 591-593 (June 1997).
- ⁸L. Muller, M. H. Hecht, L. M. Miller, H. K. Rockstad, and J. C. Lyke, "Packaging and Qualification of MEMS-Based Space Systems", *Proceedings Of the Ninth Annual International Workshop on MicroElectroMechanical Systems*, pp. 503-508, 1996.
- ⁹S. L. Miller, J. J. Sniegowski, G. LaVigne, and P. J. McWhorter, "Performance tradeoffs for a surface micromachined

microengine", *Proc. SPIE Micromachined Devices and Components II*, **Vol. 2882**, Austin October. 14-15, pp. 182-191, 1996.

¹⁰ S. L. Miller, J. J. Sniegowski, G. LaVigne, and P. J. McWhorter, "Friction in Surface Micromachined Microengines", *Proc. SPIE Smart Electronics and MEMS* **Vol. 2722**, San Diego, Feb. 28-29, 1996, pp. 197-204.

¹¹ W. Nelson, *Applied Life Data Analysis*, Chapter 9, J. Wiley & Sons, New York, 1982.

¹² W. Nelson, *Accelerated Testing*, Chapter 3, J. Wiley & Sons, New York, 1990.

¹³ D. S. Peck and O. D. Trapp, *Accelerated Testing Handbook*, Chapter 6, Technology Associates, Portola Valley, 1987.

¹⁴ Ken Peterson, Pai Targyuryorg and Daniel L. Barton "Failure Analysis for Micro-Electrical-Mechanical Systems (MEMS)", *Proc. Of International Society for Testing and Failure Analysis Symposium*, Oct. 1997, to be published.